nature astronomy

Article

https://doi.org/10.1038/s41550-023-02161-z

Determination of the equation of state from nuclear experiments and neutron star observations

Received: 22 February 2023

Accepted: 6 November 2023

Published online: 05 January 2024

Check for updates

Chun Yuen Tsang[1,2], ManYee Betty Tsang[1,2] ✉, William G. Lynch[1,2], Rohit Kumar[1] & Charles J. Horowitz[1,3]

With recent advances in neutron star observations, major progress has been made in determining the pressure of neutron star matter at high density. This pressure is constrained by the neutron star deformability, as determined from gravitational waves emitted in a neutron star merger, and measurements of the radii of two neutron stars made using the Neutron Star Interior Composition Explorer X-ray observatory on the International Space Station. Previous studies have relied on nuclear theory calculations to provide the equation of state at low density. Here we use a combination of 15 constraints composed of three astronomical observations and 12 nuclear experimental constraints that extend over a wide range of densities. Bayesian inference is then used to obtain a comprehensive nuclear equation of state. This data-centric result provides benchmarks for theoretical calculations and modelling of nuclear matter and neutron stars. Furthermore, it provides insights into the composition of neutron stars and their cooling due to neutrino radiation.

With masses that can be larger than twice the mass of the Sun and with radii of approximately 13 km, neutron stars and their observed properties raise some compelling questions[1]. Are pions, strange particles or quark matter important for understanding neutron star matter and the internal pressure that supports a neutron star and prevents it from collapsing into a black hole? If that matter is nucleonic, what roles do repulsive short-range three-neutron or four-neutron forces play in supporting the star? Understanding the connections between the pressure and the composition and structure of the stellar matter clearly constitutes a key objective for both astrophysics and nuclear physics[2]. To better understand the connections between nuclei and neutron stars[3], we combine nuclear measurements and astrophysical observations to obtain an equation of state (EOS) of nuclear matter.

The breakthrough in EOS research in the past 5 yr has been in astronomy. First, the era of multi-messenger astronomy, which involves simultaneous observations of a merging binary neutron star system with a wide array of astronomical instruments[4], has enabled more detailed studies of merging neutron stars. Then, two merging neutron stars (GW170817) observed by the Gravitational-Wave Observatories LIGO/Virgo Collaboration have provided information about the deformability of the neutron stars[5]. Next, measurements of the radii of pulsars by the Neutron Star Interior Composition Explorer (NICER)[6–9] have provided constraints on the neutron star mass–radius correlation. Both the deformability and mass–radius relationship constrain the pressure–density relationships or EOS of neutron star matter above twice the saturation density $n > 2n_0$ (refs. 10,11), where $n_0 \approx 0.16$ nucleons fm^{-3} (~2.6×14 g cm^{-3}) is the density at the core of any heavy nucleus. To augment these astrophysical constraints, we add constraints from nuclear physics experiments[12–26] obtained in the past two decades. When combined, these constraints provide a consistent description of the EOS that describes nuclear matter and neutron stars at densities of $0.5n_0 < n < 3n_0$.

[1]Facility for Rare Isotope Beams, Michigan State University, East Lansing, MI, USA. [2]Department of Physics and Astronomy, Michigan State University, East Lansing, MI, USA. [3]Center for the Exploration of Energy and Matter and Department of Physics, Indiana University, Bloomington, IN, USA. ✉e-mail: tsang@frib.msu.edu

A Bayesian analysis framework is used to infer the EOS parameters and quantify the uncertainties in the results. In addition to describing the data from nuclear physics experiments, we also use a neutron star model that employs the same EOS function to calculate neutron star properties so that these predictions can be compared to astronomical observations. The resulting EOS serves as a benchmark for microscopic nuclear theory and provides insights into the nature of strongly interacting matter in the outer core of a neutron star, its composition, and the onset of direct Urca cooling processes. In a different context, a comprehensive EOS would also yield insights into the collapse of supernovae and the emission of neutrinos.

EOS function

We assume that nucleonic matter in nuclei and in neutron stars at zero temperature shares a common nuclear EOS that can be chosen to be the energy per nucleon as a function of density $\epsilon(n)$. We can then obtain the pressure by differentiating $\epsilon(n)$ with respect to the density. We parameterize $\epsilon(n_n, n_p)$ as a function of the neutron and proton number densities n_n and n_p, where $n = n_n + n_p$ is the total nucleonic density and $\delta = \frac{n_n - n_p}{n}$ is the asymmetry. For reference, $\delta = 0$ for symmetric nuclear matter. $\delta = 1$ for pure neutron matter. For matter inside the neutron star, δ~0.9. To describe the evolution of the EOS with density and asymmetry, $\epsilon(n_n, n_p) = \epsilon_{SNM}(n) + S(n)\delta^2$ consists of two terms, where $\epsilon_{SNM}(n)$ is the energy per nucleon for symmetric nuclear matter with $\delta = 0$ and $S(n)\delta^2$ is the symmetry energy term needed when $\delta \neq 0$. This allows the EOS to describe nuclear matter with any composition of neutrons and protons. Such a division is useful because the asymmetry δ can be experimentally controlled to enhance the sensitivity to either the symmetric matter EOS or the symmetry energy term. A detailed description of the EOSs used in the Bayesian analysis can be found under Methods.

Constraints

Most experimental and astronomical observables are sensitive to the EOS over a limited range of density. For example, radii, masses and deformabilities of neutron stars largely reflect the pressure inside the neutron stars at densities of $n > 2n_0$ (refs. 10,27). On the other hand, nuclear masses and neutron skins of neutron-rich nuclei are mostly sensitive to the nuclear matter EOS at $(2/3)n_0$ (ref. 28). In addition to these two density regions, observables constructed from the distribution patterns of particles emitted in nucleus–nucleus or heavy-ion collisions (HICs) have provided constraints on the EOS at densities in the range $0.22 < n/n_0 < 4.6$ (refs. 12,13,21,22,29,30). The available data are diverse and are listed in Table 1. They are also illustrated in Fig. 1, which shows the effective density region of mostly nuclear physics constraints up to about $3n_0$. Constraints prefaced with 'HIC' were obtained from HIC experiments. A brief description of each of the constraints is given below. Recall that the nuclear EOS is parameterized into two terms, the symmetric matter term and the symmetry energy term, which accounts for the imbalance between neutrons and protons. We separate the nuclear physics constraints into those that are sensitive to the symmetry energy and those that probe the symmetric matter EOS. For astrophysics, the relevant density range is above $2n_0$.

Symmetric matter constraints

Certain properties of symmetric nuclear matter, such as the saturation density n_0 and saturation energy E_{SAT}, are reasonably well determined. We adopt the values $n_0 \approx 0.16$ fm^{-3} and $E_{SAT} \approx -16$ MeV from refs. 31,32. For the incompressibility parameter K_{SAT}, we use the values of 230 ± 30 MeV following ref. 14. Even though these three parameters are labelled in Fig. 1 at n_0, only the Taylor expansion coefficient K_{SAT} is used as a constraint in the Bayesian analysis.

Above the saturation density, measurements of the collective flow from energetic Au + Au collisions have constrained the EOS for symmetric matter at densities ranging from n_0 to $4.6n_0$ (refs. 12,13). The density range is indicated by a horizontal magenta arrow in the upper right corner of Fig. 1. The pressure–density plot for symmetric matter in Fig. 2b shows these two flow contours[12,13]. The black slanted-hatched region (HIC(DLL)) corresponds to the symmetric matter EOS published in ref. 12 from an analysis of both collective transverse and elliptical flow data measured at incident energies of 0.2–10 GeV u^{-1}. The extraction and model dependence of the HIC(DLL) contours are discussed in ref. 12 and its online supplementary material. DLL is the first letter denoting the names of the authors of[12]: Danielewicz, Lacey, Lynch. The magenta slanted-hatched region (HIC(FOPI)) constraint, obtained from FOPI Collaboration and located at lower densities, results from an independent analysis of a different set of elliptical flow measurements at 0.4–1.5 GeV u^{-1} (ref. 13). Known sources of theoretical uncertainty are modelled and the symmetric nuclear matter pressure plotted in Fig. 2b reflects this uncertainty estimation. Both contours agree very well in the region around $2n_0$ where they overlap. We take the pressure values (open square symbols) at $2n_0$ as a constraint in our analyses. In view of the availability of new and better measured data[33–35], more robust constraints on symmetric matter are expected in the near future.

Symmetry energy constraints

In the past decade, many studies have been conducted to extract the symmetry energy and its contributions to the pressure (symmetry

Table 1 | List of constraints used in the Bayesian analysis

Symmetric matter constraints				
Constraint	n (fm^{-3})	P_{SNM} (MeV fm^{-3})	K_{SAT} (MeV)	**Ref.**
HIC(DLL)	0.32	10.1±3.0		12
HIC(FOPI)	0.32	10.3±2.8		13
Giant monopole resonance	0.16		230±30	14
Asymmetric matter constraints				
Constraint	n (fm^{-3})	S(n) (MeV)	P_{sym} (MeV fm^{-3})	**Ref.**
Nuclear structure				
α_D	0.05	15.9±1.0		15
PREX-II	0.11		2.38±0.75	16,17,28
Nuclear mass constraints				
Mass(Skyrme)	0.101±0.005	24.7±0.8		18,28
Mass(DFT)	0.115±0.002	25.4±1.1		19,28
Isobaric analogue states	0.106±0.006	25.5±1.1		20,28
HIC constraints				
HIC(isodiff)	0.035±0.011	10.3±1.0		21,28
HIC(n/p ratio)	0.069±0.008	16.8±1.2		22,28
HIC(π)	0.232±0.032	52±13	10.9±8.7	23,28
HIC(n/p flow)	0.240		12.1±8.4	24–26,28
Astronomical constraints				
Constraint	M (⊙)	R (km)	Λ	**Ref.**
LIGO	1.4		190^{+390}_{-120}	11
*Riley PSR J0030+0451	$1.34^{+0.15}_{-0.16}$	$12.71^{+1.14}_{-1.19}$		6
*Miller PSR J0030+0451	$1.44^{+0.15}_{-0.14}$	$13.02^{+1.24}_{-1.06}$		7
*Riley PSR J0740+6620	$2.07^{+0.07}_{-0.07}$	$12.39^{+1.30}_{-0.98}$		8
*Miller PSR J0740+6620	$2.08^{+0.07}_{-0.07}$	$13.7^{+2.6}_{-1.5}$		9

The NICER constraints marked with asterisks (*) are given half weight in the Bayesian analysis as the four constraints listed here come from two measurements analysed by two different groups.

https://doi.org/10.1038/s41550-023-02161-z

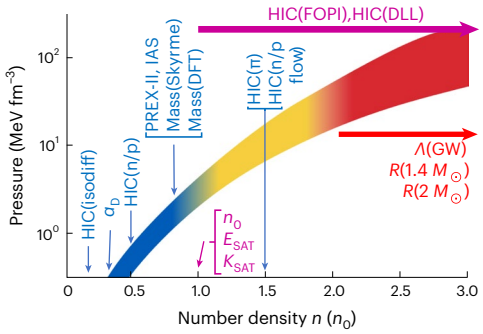

Fig. 1 | Constraints from nuclear experiments and astronomy observations with their corresponding sensitive densities. The red horizontal arrow indicates the high-density region (>2n_0) probed by neutron star observations. The magenta text indicates chosen values of $E_{SAT} \approx -16$ MeV for the symmetric matter EOS located at the saturation density $n_0 \approx 0.16$ fm^{-3} following refs. 31,32 and a symmetric matter constraint on K_{SAT} obtained from studies of giant monopole resonance[14]. The purple horizontal arrow at the top of the figure indicates the density range from symmetric matter constraints from HIC studies[12,13]. The remaining terrestrial constraints for nuclear symmetry energy or symmetry pressure are labelled in blue and positioned at their sensitive densities[28]. The coloured band indicates the approximate dependence of pressure on density for pure neutron matter from the findings of current work. DFT, density functional theory; GW, gravitational wave; IAS, isobaric analogue states; isodiff, isospin diffusion n/p ratio, neutron to proton yield ratios; n/p flow, neutron to proton differential flow; DDL, Danielewicz, Lacey, Lynch, the authors of Ref. [12]; FOPI, FOPI Collaboration.

pressure)[28], mostly at low densities. The precise symmetry energy constraints shown in Fig. 2d have been obtained at about (2/3)n_0 from nuclear masses using density functional theory in two independent analyses involving different nuclei labelled as Mass(Skyrme)[18] and Mass(DFT)[19]. In this density region, we also have precise constraints obtained from the energies of isobaric analogue states[20] indicated by a data point labelled as IAS. Measurements of the dipole polarizability of ^{208}Pb provide a constraint at a lower density of $n = 0.05$ fm^{-3}, which is labelled as α_D (ref. 15). Values for the neutron skin thickness and the slope of the symmetry energy $L(2n_0/3)$ at (2/3)n_0 have been published for the PREX-II experiment, from which we obtain the pressure $P(2n_0/3)$. This is labelled as PREX-II (refs. 16,17) in Fig. 2a.

HICs have been used to probe the symmetry energy and pressure at densities far from (2/3)n_0. At incident energies below 100 MeV per nucleon, lower densities are probed when matter expands after initial impact and compression of the projectile and target. Experimental observables primarily reflect the symmetry energy at subsaturation densities with $n \ll n_0$ (refs. 21,22). Constraints from isospin diffusion in Sn + Sn collisions, labelled as HIC(isodiff)[21], provide a constraint at $n/n_0 = 0.22 \pm 0.07$. Ratios of neutron and proton energy spectra in central collisions, labelled as HIC(n/p), provide a constraint on the symmetry energy at $n/n_0 = 0.43 \pm 0.05$ (ref. 22).

Higher energy (>200 MeV u^{-1}) central HICs probe the EOS at $n > n_0$. The HIC(n/p flow) data point comes from the elliptical collective flows of neutrons and hydrogen nuclei in Au + Au collisions[24–26]. HIC(π) comes from a recent measurement of the spectral ratios of charged pions in very neutron-rich ^{132}Sn + ^{124}Sn collisions and nearly symmetric ^{108}Sn + ^{112}Sn collisions[23]. The use of (^{132}Sn) and (^{108}Sn) radioactive beams have enhanced the asymmetry variation and the experimental sensitivity to the symmetry energy. The uncertainty of the pion constraint reflects large uncertainties in the difference between neutron and proton effective masses and in the contributions from non-resonant pion production[23]. Extractions and discussions of the model-dependent uncertainties in the constraint marked as HIC(FOPI), HIC(n/p) and HIC(n/p flow) can be found in refs. 13,23,24. Finally, note that the uncertainties in the sensitive densities listed in Table 1 are too small to influence the final EOS results and, therefore, are not used in the Bayesian analysis.

Constraints from astronomical observations

When two neighbouring neutron stars begin to merge, the gravitational field of each neutron star induces a tidal deformation in the other. The influence of the EOS of neutron stars on the gravitational-wave signal during the in-spiral phase is encoded in the dimensionless, neutron star tidal deformability Λ (ref. 5). In the inset of Fig. 2c, the value of Λ for 1.4 $M_\odot$ obtained from the binary neutron star merger event of GW170817 (ref. 11) is plotted. The observation of a later merger event (GW190425) did not improve the accuracy of Λ due to poorer observing conditions[36].

Since its operation in 2019, NICER has measured the radii of two pulsars with very different masses[6–9]. Figure 2c shows values for the radii obtained by Riley et al.[6,8] and Miller et al.[7,9] for these two pulsars, PSR J0030+0451 and PSR J0740+6620 (refs. 37,38) with measured masses of $1.34^{+0.15}_{-0.16}$ $M_\odot$ ($1.44^{+0.15}_{-0.14}$ $M_\odot$) and $2.07^{+0.07}_{-0.07}$ $M_\odot$ ($2.08^{+0.07}_{-0.07}$ $M_\odot$), respectively[6–9]. Since these are independent analyses of the same pulsars, each constraint is given the weight of 0.5 in the analysis.

Description of the neutron star model calculations

We adopt the neutron star model described in ref. 39 to calculate the properties of a neutron star, such as its deformability, mass and radius, for each EOS in the prior distribution, by solving the Tolman–Oppenheimer–Volkoff (TOV) equation[40,41]. In particular, we focus on the impact of the EOS on the outer core of the neutron star where neutrons comprise the bulk of the matter and the inclusion of small admixtures of protons, electrons and muons is required to attain β equilibrium. For simplicity, we do not include sharp phase transitions within the neutron star core. Both the inner and outer cores are described by the same equation except when the speed of sound in the outer core EOS begins to exceed the speed of light. If this occurs, we transition it to the stiffest possible EOS for which speed of sound equals the speed of light and the EOS becomes very repulsive. Such transitions occur mostly above 3n_0. Below the crust–core transition density, we use the crustal EOS of ref. 42 (see Methods for details). Our study provides insights into the EOS at densities of 0.5–3n_0 for which the current experimental constraints are relevant.

Results

Bayesian inference is used to simultaneously determine all the parameters used in the EOS constructed from metamodelling (see Methods for details). We constrain the Taylor expansion coefficients of the EOS solely by the 15 discrete constraints obtained from astronomical observations and nuclear physics experiments. These constraints are plotted in Fig. 2a–d (n_0 and E_{SAT} are fixed parameters, not constraints) and listed in Table 1. The availability of so many constraints precludes the dominance of a single experiment, observation or theory and provides data over a wide range of densities.

The posterior distributions of the EOS calculated from Bayes theorem are shown in Fig. 2. The 68% and 95% confidence intervals (CIs) of the posteriors are represented by the dark green and light blue shaded regions. In each case, the posterior uncertainties are much narrower than that of the prior (indicated by the blue dashed curves) and nearly all data fall within the 95% CI of the posterior regions. The posterior of the density dependence of the symmetry energy shown in Fig. 2d is similar to that obtained in ref. 28 but with much narrower uncertainty bands due to the additional astrophysical constraints included in the present work.

In Fig. 2f, the purplish-blue shaded area shows the EOS for neutron star matter at 90% CI obtained by employing only astronomical constraints[10]. The uncertainty of our extracted EOS is narrower, especially in the low-density region where we employ experimental data. At high density, the difference in uncertainties may be due to the different

https://doi.org/10.1038/s41550-023-02161-z

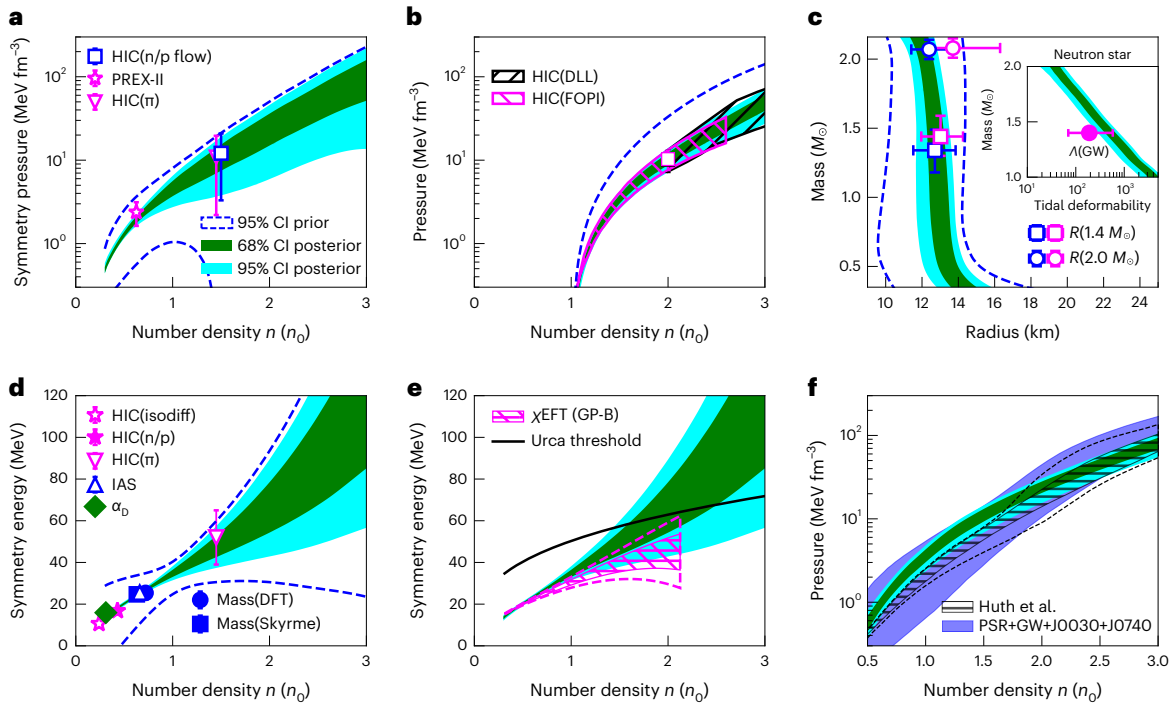

Fig. 2 | Constraints on and posteriors of the nuclear EOS and neutron star. All symbols represent data discussed in the text and listed in Table 1. The error bars reflect 1σ standard deviation unless specified. The blue dashed lines are 95% CI boundaries of the prior distributions with an initial sample size of 1.5 million. The boundaries of the dark green and light blue shaded regions represent 68% and 95% CI boundaries of the posterior distributions, respectively, using an initial size of 3 million. **a**, Density dependence of the symmetry pressure. **b**, Density dependence of the symmetric nuclear matter pressure. **c**, Mass–radius correlation. Symbols are data from two independent analyses of two pulsars measured by NICER. The inset shows the mass–deformability correlation. The symbol represents the experimental deformability value for 1.4 $M_\odot$ with error bars reflecting 90% CI. **d**, Density dependence of the symmetry energy. **e**, Density dependence of the symmetry energy compared to χEFT(GP-B) calculations (magenta). The Gaussian process–BUQEYE collaboration (GP-B) is a version of χEFT calculations used in this work. The onset of Urca cooling occurs above the solid black line. **f**, Density dependence of the pressure for neutron star matter. The purplish-blue area is the EOS obtained in ref. 10 based on astronomical constraints using only a non-parametric EOS. The hatched area is from[43] with astronomical and high-density HIC constraints at high energy and χEFT as priors at low density.

algorithm used in the analysis. Reference [10] adopts non-parametric EOSs as priors whereas in the current work we use parametric priors based on an expansion widely used in nuclear physics. The recent constraints[43] obtained by incorporating the chiral effective field theory (χEFT) at low density and Au + Au collective flow data from refs. 13,24,26 are shown as the hatched regions (black dashed lines) corresponding to 68% (95%) CI. The differences between the current work and ref. 43 most probably arise from its strict reliance on the χEFT EOS below 1.5n_0, which produces a softer EOS. More comparisons with χEFT results are discussed below.

Implications

Composition and the Urca cooling of neutron stars

Data on the pressure of both symmetric matter and neutron-rich matter provide crucial insights into the composition of dense matter. The symmetry energy is very important for understanding the composition and dynamics of matter within neutron stars because it contributes to the chemical potentials of the particles that compose the stellar matter. A large symmetry energy may increase the fraction of protons, muons, hyperons or other particles that are present in dense matter. In β equilibrium, the proton fraction (protons per baryon) y_p increases with increasing symmetry energy. (Details for calculating y_p are given in Methods.)

If y_p is large enough, the Urca process of rapid neutrino emission may quickly cool a neutron star[44]. Many isolated neutron stars have been observed to be cooling relatively slowly, so the Urca process is probably not operating[45]. However, some neutron stars, perhaps the more massive ones, have been observed to be cooling quickly, consistent with Urca[46] process.

In the Urca process, a neutron undergoes beta decay, which is followed by the proton capturing the electron with the net effect of radiating a $\nu\bar{\nu}$ neutrino pair that cools the star. To conserve both momentum and energy in these weak interactions, the Fermi momenta of protons k_F^p, neutrons k_F^n and electrons k_F^e must satisfy $k_F^p + k_F^e > k_F^n$. At a given density n, a symmetry energy above the black solid line in Fig. 2e will have a large enough y_p to satisfy this condition so that the Urca process is potentially allowed. Note that the composition shown in Fig. 3a was made possible by combining symmetric nuclear matter data and symmetry energy data from HICs. When the central density n_{cen} of a neutron star of mass $M(M_\odot)$ exceeds the Urca threshold density n_{Urca}, the star can potentially cool quickly through the Urca process. Figure 3b shows the mass dependence of $(n_{cen} - n_{Urca})$, indicating that Urca cooling is probable for stars with a mass larger than 1.8 $M_\odot$. Note that neutron star cooling depends on possible superfluid pairing gaps in addition to y_p. See, for example, ref. 47. Furthermore, matter in the deep interior of a neutron star may not mainly consist of nucleons. In this simple discussion, we do not include such effects.

Benchmarking microscopic theories

The EOS extracted in this work provides the energy per nucleon of symmetric matter $\epsilon_{SNM}(n)$ and the symmetry energy term $S(n)$. The sum of these two terms yields the pure neutron matter EOS $\epsilon_{PNM}(n)$. Unlike previous studies[43,48,49], our methodology does not require input from any theoretical EOS. With recent advances made in the quantification of the uncertainties of χEFT (ref. 50), it has been extended to $2n_0$ and has become a popular choice as a low-density EOS for describing neutron star properties[43,48,49]. Thus, it is interesting to compare our

https://doi.org/10.1038/s41550-023-02161-z

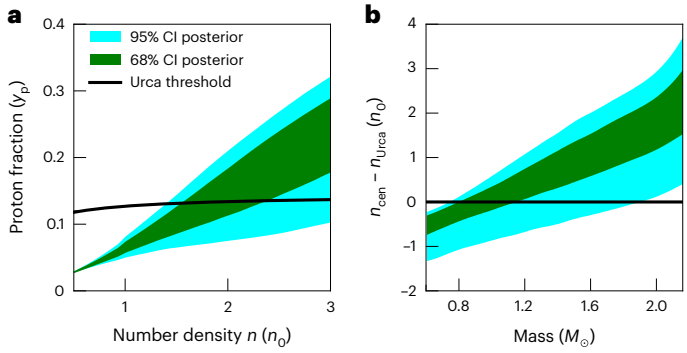

Fig. 3 | Predictions on the proton fraction and the Urca cooling. The boundaries of the dark green and light blue shaded regions represent 68% and 95% CI boundaries of the posterior distributions, respectively, using an initial sample size of 3 million. **a**, Density dependence of the proton fraction. The onset of Urca cooling occurs above the solid black line. **b**, Density difference between central density n_{cen} of a neutron star of mass M and the lowest density n_{Ucra} for which the Urca process is allowed. The y axis is in units of saturation density n_0. If this density difference is greater than zero, the star may potentially cool quickly.

results with the theoretical calculations. In Fig. 4, we compare the constrained EOS to the χEFT(GP-B) calculations with the 500 MeV momentum cutoff[31,50,51] for the symmetry energy term of the EOS (left panels), symmetric nuclear matter term (middle panels) and for pure neutron matter (right panels) both in terms of pressure versus density (upper panels) and energy per nucleon versus density (lower panels). Note that there are different implementations of χEFT. The χEFT(GP-B) used here is based on Gaussian Process from the BUQEYE Collaboration. It has a truncation that is fully quantified as shown by the solid magenta contours corresponding to the 95% CI and the magenta hatched region corresponding to the 68% CI.

In general, the extracted EOS is broadly consistent with χEFT calculations especially at densities below n_0. For the symmetric nuclear matter, the agreement is rather good up to $1.5n_0$ even though it is slightly offset from the saturation energy and saturation density, as noted in ref. 51. To compare the symmetry term of the EOS, the symmetry energy (pressure) of the χEFT(GP-B) EOS was obtained by subtracting the energy (pressure) of the symmetric matter from that of the pure neutron matter[31,50,51]. This leads to large uncertainty bands in Fig. 4a,d. The EOS derived from χEFT is, in general, softer, consistent with the smaller predicted neutron star radii[43]. Interestingly, due to the softness of the χEFT, the Urca process will be mostly disallowed in neutron star matter utilizing χEFT as EOS, as shown in Fig. 4d, where the black line indicates the Urca threshold.

Summary

In summary, we perform Bayesian analyses of 12 nuclear experimental constraints with three complementary constraints from astronomical observation to obtain a consistent understanding of the EOS of neutron-rich matter at number densities from about half to three times the saturation density. Our method eliminates any over-reliance on the data from one particular experiment, observation or theory. Within the density range we study, the data do not appear to require the existence of a phase transition inside the core of neutron stars nor do they rule them out. We adopt an EOS constructed from metamodelling in the form of a Taylor expansion around the saturation density up to fourth order. The extracted values of the expansion coefficients allow the construction of the EOS for symmetric and asymmetric matter including neutron star matter. Even though there are broad agreements between our results and χEFT, especially at low density where the theory is more valid, the disagreement increases with density. The symmetry energy component of the EOS allows a determination of the thresholds for Urca cooling. With the neutron star EOS, we obtained a radius of $12.9^{+0.4}_{-0.5}$ km and a deformability of 530^{+115}_{-138} for the canonical neutron star with 1.4 solar mass. We found that a heavy-mass neutron

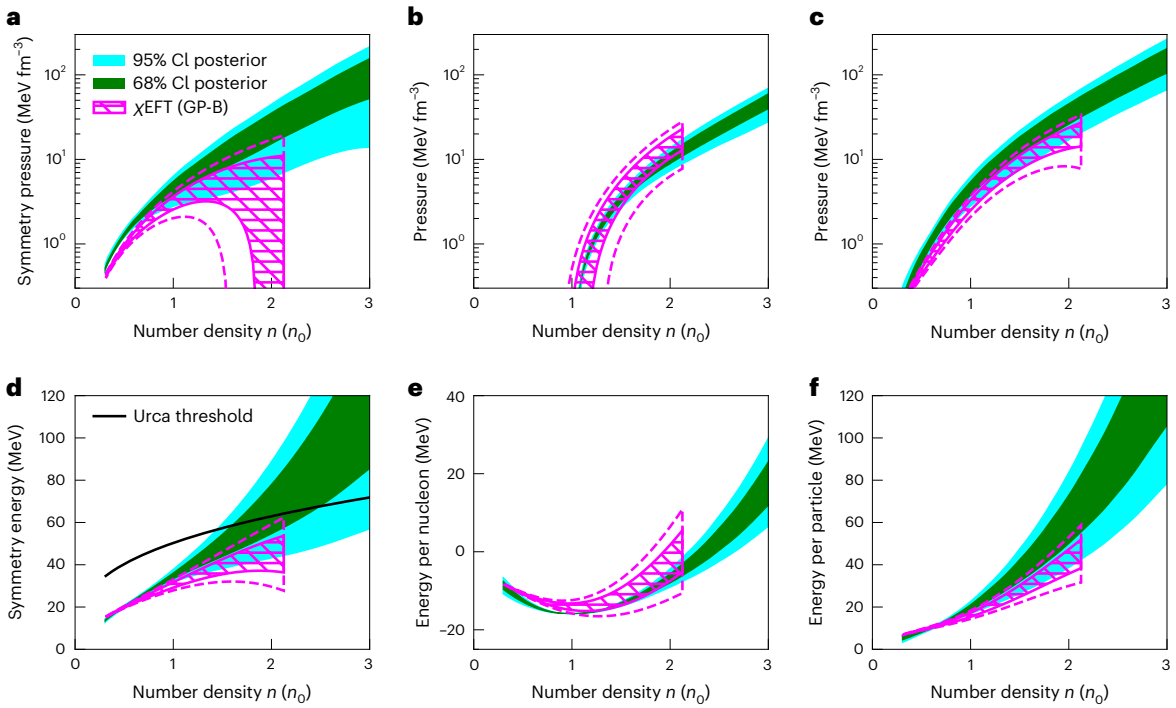

Fig. 4 | Energy and pressure of symmetry energy, symmetric matter and pure neutron matter. a–**c**, Symmetry pressure (**a**), pressure of symmetric nuclear matter (**b**) and pressure of pure neutron matter (**c**) as functions of the number density n. **d**–**f**, Symmetry energy (**d**), energy per nucleon of symmetric nuclear matter (**e**) and energy per nuclear of pure neutron matter (**f**) as functions of the number density. The solid green (light blue) region is the 68% (95%) CI of the posteriors using an initial sample size of 3 million events. The magenta (hatched) contours represent the calculations from χEFT(GP-B) based on Gaussian Process from the BUQEYE Collaboration (refs. 31,50,51).

star cools quickly by the Urca process. The tension between the posteriors and the data nominally reveals areas where improved measurements are needed. This includes additional measurements of the tidal deformability of neutron stars and more precise heavy-ion data for the symmetry energy and pressure above the saturation density[52].

Methods

Parameterization of the EOS and the neutron star model

Neutron star radii and deformabilities can be combined to provide constraints on matter at densities of $2 < n/n_0 < 4$ in the outer core of a cold neutron star[8,9,11] where we assume that the hadronic component of matter is largely nucleons (neutrons and protons). Experimental observables that probe the EOS with nucleus–nucleus collisions provide constraints on nucleonic EOS functionals that can be used to describe such densities[12,13,23,24]. To perform these calculations, we express the dominant hadronic component of the EOS in terms of the energy per nucleon $\epsilon(n,\delta)$ or pressure, $P = n^2\partial\epsilon/\partial n$, where $n = n_n + n_p$ is the total density, n_n and n_p are the neutron and proton number densities and $\delta \equiv (n_n - n_p)/n$ is the asymmetry.

To second order in δ, the energy $\epsilon(n,\delta)$ can be written as[53]

$$\epsilon(n,\delta) \approx \epsilon(n,0) + \delta^2 S(n), \tag{1}$$

where $\epsilon(n,0)$, is the energy per nucleon of symmetric matter with equal neutron and proton densities (that is $\delta = 0$) and $S(n)$, is the symmetry energy of pure neutron matter for which $\delta = 1$. For reference, $\delta \sim 0.9$ in neutron star. We calculate the symmetric matter EOS ($\epsilon(n,0)$) and the density dependence of the symmetry energy ($S(n)$) using the metamodelling ELFc formalism of ref. 54. In metamodelling, both $\epsilon(n,0)$ and $S(n)$ contain kinetic energy (K.E.) and mean-field potential terms (U), as well as effective mass (m^*) corrections that reflect the non-localities of the nucleonic mean-field potentials. These effective mass corrections appear in the kinetic energy term such that the mass term is replaced by effective masses:

$$\epsilon(n,\delta) = \text{K.E.}(n,\delta,m^*) + U(n,\delta). \tag{2}$$

Away from $n = 0$ where the kinetic energy has a branch cut singularity, the metamodelling EOS is dominated by the values and derivatives of $\epsilon(n,0)$ and $S(n)$ at the saturation density $n_0 \approx 0.16$ nucleons fm^{-3}, which are labelled as follows:

$$\begin{aligned} &E_{\rm SAT} = \epsilon(n_0,0), K_{\rm SAT} = \frac{1}{2!}\frac{\mathrm{d}^2\epsilon(n,0)}{\mathrm{d}x^2}|_{n=n_0}, \\ &Q_{\rm SAT} = \frac{1}{3!}\frac{\mathrm{d}^3\epsilon(n,0)}{\mathrm{d}x^3}|_{n=n_0}, Z_{\rm SAT} = \frac{1}{4!}\frac{\mathrm{d}^4\epsilon(n,0)}{\mathrm{d}x^4}|_{n=n_0}, \end{aligned} \tag{3}$$

$$\begin{aligned} &S_0 = S(n_0), L = \frac{\mathrm{d}S(n)}{\mathrm{d}x}|_{n=n_0}, K_{\rm sym} = \frac{1}{2!}\frac{\mathrm{d}^2S(n)}{\mathrm{d}x^2}|_{n=n_0}, \\ &Q_{\rm sym} = \frac{1}{3!}\frac{\mathrm{d}^3S(n)}{\mathrm{d}x^3}|_{n=n_0}, Z_{\rm sym} = \frac{1}{4!}\frac{\mathrm{d}^4S(n)}{\mathrm{d}x^4}|_{n=n_0}, \end{aligned} \tag{4}$$

where $x = (n - n_0)/(3n_0)$. The exact formulae for these coefficients and how they are combined with additional correction terms to obtain the EOS down to $n = 0$ can be found in ref. 54.

By using an EOS of the metamodelling form[54] instead of the more customary Skyrme[14] or relativistic mean-field[55] density functionals, which are commonly used to describe nuclei and nuclear matter, we can reduce the model-dependent correlations in the asymptotic expansion coefficients associated with equations (3) and (4) that are characteristic features of the Skyrme and relativistic mean-field functionals[54]. This allows the influence of the experimental and astrophysical constraints to be modelled more flexibly and clearly. Even though the nucleon effective mass m^*/m_0 can be an adjustable parameter in the metamodelling approach[54], we assigned nominal values of $m^*/m_0 = 0.7$ and $m_s^* = m_v^*$, where m_s^* and m_v^* are the isoscalar and isovector effective masses, respectively.

We adopted the metamodelling EOS for nuclear matter in the outer core of a neutron star, which is composed of neutrons, protons, electrons and muons, and is β equilibrated at a temperature close to zero mega-electronvolts. Consistent with our experiment- and observation-driven approach, we did not introduce a theoretical model for a different form for matter in the inner core of a neutron star but looked to see if strong signatures for its presence can be observed by changes in the EOS at high densities, which might emerge in the analyses. We found none. We did ensure that when we extended the EOS to higher densities that the speed of sound c_s ($= c\sqrt{\partial P/\partial\epsilon}$) remains less than the speed of light c.

To calculate a neutron star radius, we need to extend the EOS from the core to the crust. We adopted a commonly used EOS for the solid outer crust from ref. 42 and extrapolated this through the inner crust region of $0.3n_T < n < n_T$ with spline interpolations. Here, $n_T = -3.75 \times 10^{-4}L + 0.0963$ fm^{-3} is the crust to core transition density. In ref. 39, the uncertainty of this crustal EOS description is estimated to be small compared to the present uncertainty of the EOS in the core of a neutron star. Using these EOS expressions, neutron star properties, such as deformability, masses and radii, have been obtained by solving the TOV equations[40,41]. More details of the neutron star model and its uncertainties are provided in ref. 39.

Bayesian analysis

Priors. A Bayesian analysis was used to constrain the relevant Taylor expansion coefficients defined in equations (3) and (4). Supplementary Table 1 lists the range of parameters used to generate the priors that cover most of the experimental and astrophysical constraints listed in Table 1. For comparison, the corresponding posterior values are also listed in Supplementary Table 1. Here, we give the rationale for choosing the ranges of the listed parameters using experimental information as guidance when possible. The general principle is to give each parameter a very wide range to ensure that the priors encompass as much of the experimental constraints as possible.

The ranges of the symmetry energy parameters of equation (4) are guided by the comprehensive study in ref. 28. We do not have a corresponding comprehensive analysis for the symmetric matter EOS parameters of equation (3). Together with the well-known values of n_0, $E_{\rm SAT}$ and $K_{\rm SAT}$, the existence of two consistent constraints at $2n_0$ on the symmetric matter EOS provides some guidance on the EOS up to $2n_0$.

Analyses of recent experimental results at high collision energy and, therefore, high density from the Hades collaboration[56] and from the Beam Energy Scan Collaboration[34,35] have revealed disagreements between the new data and data from the E895 Collaboration[57,58]. The latter was used to derive the HIC(DLL) contours. The new data have stimulated a re-evaluation of the EOS for symmetric matter[59] at high density, which may lead to a future re-evaluation of the pressure constraints currently provided by HIC(DLL) at densities greater than $3n_0$. For the prior distributions of the symmetric matter EOS in this work, we assessed both the existing HIC(DLL) and new but still preliminary analysis[59] and concluded that the symmetric matter pressure at $4n_0$ does not exceed 300 MeV fm^{-3}. We include this knowledge in the prior distribution by selecting values for $Z_{\rm SAT}$ such that the symmetry pressure $P_{\rm SNM}(4n_0)$ is uniformly distributed from 0 to 300 MeV fm^{-3}, nearly twice the published HIC(DLL) standard deviation upper limit of 156 MeV fm^{-3} (ref. 12). Effectively, this means that the $Z_{\rm SAT}$ prior is not independent but is correlated with the priors for other Taylor coefficients, especially $Q_{\rm SAT}$, in the expression for the symmetric matter EOS. Thus, $P_{\rm SNM}(4n_0)$ appears in Supplementary Table 1 instead of $Z_{\rm SAT}$. The current prior distributions are wide enough to encompass possible higher pressures from the preliminary analysis in refs. 59

To illustrate the influence of neutron star on the priors, 5,000 randomly chosen priors based on the parameter ranges listed in Supplementary Table 1 are shown as grey curves in Supplementary Fig. 1. Panel 1a shows the density dependence of energy per particle of the

pure neutron matter (as commonly used by the nuclear physics community) whereas Panel 1b shows the corresponding pressure as a function of number density (more commonly used by the astrophysics community). The TOV equations are solved and any EOSs that do not lead to a maximum neutron star mass of at least 2.17 $M_\odot$ are rejected before applying the Bayesian analysis. (Lowering the least maximum neutron star mass to 1.8 $M_\odot$ does not change the results or conclusions.) The neutron star requirement removes very stiff and very soft EOSs, especially those with a very small or negative pressure at high density. This greatly reduces the number of priors to about 5% of the original numbers. They are shown as blue curves in Supplementary Fig. 1. Since these are the priors used in the Bayesian analysis, they will be referred to simply as 'priors' from here on.

Bayes theorem. Bayesian inference is performed to generate the posterior distribution, which is governed by various expansion coefficients defined in equations (3) and (4) and the experimental and astronomical measurements. The posterior distribution is given by Bayes theorem[60], which can be written as

$$P(\text{EOS}|\text{Constraints}) \propto P(\text{EOS}) \prod_i \mathcal{L}(i\text{th constraint}). \quad (5)$$

In this equation, P(EOS) is the prior and $\mathcal{L}(i\text{th constraint})$ is the likelihood, defined as the probability of observing the experimental and astronomical results assuming that a given set of EOS expansion coefficients is the perfect description of nuclear matter. In this analysis, for an observable O, which the measurements/observations constrain to have a mean of x_0 and a standard deviation σ equal to the error, the likelihood of it having a true value of x is given by a Gaussian $\exp[-(x-x_0)^2/(2\sigma^2)]$.

For gravitational wave constraints with asymmetric uncertainty, an asymmetric Gaussian is used. The latter is constructed from two Gaussian functions with the same mean value but different widths and scaled to match the height of each other at the mean. These are used to describe the two halves of the distribution on opposite sides of the mean value.

Posterior distributions. The Bayesian analysis is performed with the parameters allowed to vary within the ranges listed in Supplementary Table 1. The posteriors of the EOS parameters and predictions for the radius and deformability of the 1.4 $M_\odot$ neutron star are also listed. In the same table, we list the predictions for the Taylor expansion coefficients for the symmetry energy at a density of 0.1 fm^{-3} for which the experimental constraints are most robust. A parameter is defined as a variable that is an input to an EOS whereas a prediction is defined as everything is calculated. We made this distinction for in tables for clarity, but they are all called parameters in other sections of this article for brevity.

The posterior distribution, which describes the probability of the ith parameter having value m_i given the constraints listed in Table 1, was calculated from Bayes theorem. The marginalized posterior distributions were calculated by distributing each parameter on a histogram, weighted by a factor from equation (5). A total of 4.5 million EOSs were sampled in two stages. In the first stage, 1.5 million EOSs were sampled uniformly within the ranges in Supplementary Table 1. This small set of expansion coefficients informed us of the range of preferred values. The remaining 3 million EOSs were sampled uniformly within 99% CIs from the marginalized distributions from the initial batch of EOSs. This two-step process allowed us to more efficiently sample the parameter space that is relevant. The CIs for the energy and pressure values for the EOS, as well as the values of various observables directly related to the nuclear EOS, were calculated by weighting each prediction with the corresponding factor.

Supplementary Fig. 2 shows corner correlation plots for six parameters: the symmetry energy at the saturation density S_0, the slopes of the symmetry energy at $0.67n_0$, n_0 and $1.5n_0$, and the radii and deformability of a neutron star with a nominal mass of 1.4 $M_\odot$. In red, we show the 1σ and 2σ contours of these correlations. Because we constructed the prior EOS using metamodelling, we avoid any a priori correlations between the slope of the symmetry energy at different densities and other neutron star properties. The correlations in these plots reflect strong connections between the EOS at specific densities and neutron star radii and deformabilities. Nonetheless, both the radii and deformability of the neutron star are correlated with the slope of the symmetry energy at $0.67n_0$, n_0 and $1.5n_0$ as well as with each other, consistent with previous studies. Along the diagonal are the posterior one-dimensional plots for the parameters with the solid vertical lines corresponding to the median (50th percentile) and the dashed vertical lines corresponding to the 68% (1σ) CI. The posterior values with 1σ uncertainties are also listed in Supplementary Table 1. In each case, the posterior uncertainties are much narrower than that of the prior.

Direct Urca cooling

The symmetry energy is very important for understanding the composition and dynamics of matter within neutron stars because it contributes to the chemical potentials of the particles that compose the stellar matter. In β equilibrium, the chemical potentials of a neutron μ_n, a proton μ_p and an electron μ_e satisfy $\mu_e = \mu_n - \mu_p$ and the proton fraction y_p satisfies

$$[4S(n)(1-2y_p)]^3 + \left\{[4S(n)(1-2y_p)]^2 - m_\mu^2\right\}^{3/2} = 3\pi^2 n y_p, \quad (6)$$

at baryon density n with m_μ being the muon mass.

Data availability

All data points used in this work are listed in Table 1 together with the references. They are also plotted in Fig. 2.

Code availability

Analysis codes specially written for this work are available online at https://github.com/nscl-hira/TidalPolarizabilityPublic. The TOV solver used in this work is available upon request to the corresponding author.

References

1. Lattimer, J. M. & Prakash, M. The physics of neutron stars. *Science* **304**, 536–542 (2004).
2. Dietrich, T. et al. Multimessenger constraints on the neutron-star equation of state and the Hubble constant. *Science* **370**, 1450–1453 (2020).
3. Hen, O. From nuclear clusters to neutron stars. *Science* **371**, 232–232 (2021).
4. Abbott, B. P. et al. Multi-messenger observations of a binary neutron star merger. *Astrophys. J. Lett.* **848**, L12 (2017).
5. Abbott, B. P. et al. GW170817: observation of gravitational waves from a binary neutron star inspiral. *Phys. Rev. Lett.* **119**, 161101 (2017).
6. Riley, T. E. et al. A NICER view of PSR J0030+0451: millisecond pulsar parameter estimation. *Astrophys. J. Lett.* **887**, L21 (2019).
7. Miller, M. C. et al. PSR J0030+0451 mass and radius from NICER data and implications for the properties of neutron star matter. *Astrophys. J.* **887**, L24 (2019).
8. Riley, T. E. et al. A NICER view of the massive pulsar PSR J0740+6620 informed by radio timing and XMM-Newton spectroscopy. *Astrophys. J. Lett.* **918**, L27 (2021).
9. Miller, M. C. et al. The radius of PSR J0740+6620 from NICER and XMM-Newton data. *Astrophys. J. Lett.* **918**, L28 (2021).
10. Legred, I., Chatziioannou, K., Essick, R., Han, S. & Landry, P. Impact of the PSR J0740+6620 radius constraint on the properties of high-density matter. *Phys. Rev. D* **104**, 063003 (2021).

11. Abbott, B. P. et al. GW170817: measurements of neutron star radii and equation of state. *Phys. Rev. Lett.* **121**, 161101 (2018).
12. Danielewicz, P., Lacey, R. & Lynch, W. G. Determination of the equation of state of dense matter. *Science* **298**, 1592–1596 (2002).
13. Le Fevre, A., Leifels, Y., Reisdorf, W., Aichelin, J. & Hartnack, C. Constraining the nuclear matter equation of state around twice saturation density. *Nucl. Phys. A* **945**, 112–133 (2016).
14. Dutra, M. et al. Skyrme interaction and nuclear matter constraints. *Phys. Rev. C* **85**, 035201 (2012).
15. Zhang, Z. & Chen, L.-W. Electric dipole polarizability in ^{208}Pb as a probe of the symmetry energy and neutron matter around $\rho_0/3$. *Phys. Rev. C* **92**, 031301 (2015).
16. Adhikari, D. et al. Accurate determination of the neutron skin thickness of ^{208}Pb through parity-violation in electron scattering. *Phys. Rev. Lett.* **126**, 172502 (2021).
17. Reed, B. T., Fattoyev, F. J., Horowitz, C. J. & Piekarewicz, J. Implications of PREX-2 on the equation of state of neutron-rich matter. *Phys. Rev. Lett.* **126**, 172503 (2021).
18. Brown, B. A. Constraints on the Skyrme equations of state from properties of doubly magic nuclei. *Phys. Rev. Lett.* **111**, 232502 (2013).
19. Kortelainen, M. et al. Nuclear energy density optimization: large deformations. *Phys. Rev. C* **85**, 024304 (2012).
20. Danielewicz, P., Singh, P. & Lee, J. Symmetry energy III: isovector skins. *Nucl. Phys. A* **958**, 147–186 (2017).
21. Tsang, M. B. et al. Constraints on the density dependence of the symmetry energy. *Phys. Rev. Lett.* **102**, 122701 (2009).
22. Morfouace, P. et al. Constraining the symmetry energy with heavy-ion collisions and Bayesian analyses. *Phys. Lett. B* **799**, 135045 (2019).
23. Estee, J. et al. Probing the symmetry energy with the spectral pion ratio. *Phys. Rev. Lett.* **126**, 162701 (2021).
24. Cozma, M. Feasibility of constraining the curvature parameter of the symmetry energy using elliptic flow data. *Eur. Phys. J. A* **54**, 1–23 (2018).
25. Russotto, P. et al. Symmetry energy from elliptic flow in ^{197}Au+^{197}Au. *Phys. Lett. B* **697**, 471–476 (2011).
26. Russotto, P. et al. Results of the ASY-EOS experiment at GSI: the symmetry energy at suprasaturation density. *Phys. Rev. C* **94**, 034608 (2016).
27. Miller, M. C., Chirenti, C. & Lamb, F. K. Constraining the equation of state of high-density cold matter using nuclear and astronomical measurements. *Astrophys. J.* **888**, 12 (2019).
28. Lynch, W. & Tsang, M. Decoding the density dependence of the nuclear symmetry energy. *Phys. Lett. B* **830**, 137098 (2022).
29. Tsang, M. B. et al. Isospin diffusion and the nuclear symmetry energy in heavy ion reactions. *Phys. Rev. Lett.* **92**, 062701 (2004).
30. Tsang, M. B. et al. Constraints on the symmetry energy and neutron skins from experiments and theory. *Phys. Rev. C* **86**, 015803 (2012).
31. Drischler, C., Hebeler, K. & Schwenk, A. Chiral interactions up to next-to-next-to-next-to-leading order and nuclear saturation. *Phys. Rev. Lett.* **122**, 042501 (2019).
32. Drischler, C., Hebeler, K. & Schwenk, A. Asymmetric nuclear matter based on chiral two- and three-nucleon interactions. *Phys. Rev. C* **93**, 054314 (2016).
33. Adamczewski-Musch, J. et al. Directed, elliptic, and higher order flow harmonics of protons, deuterons, and tritons in Au+Au collisions at $\sqrt{s_{NN}} = 2.4$ GeV. *Phys. Rev. Lett.* **125**, 262301 (2020).
34. Abdallah, M. S. et al. Flow and interferometry results from Au+Au collisions at $\sqrt{s_{NN}} = 4.5$ GeV. *Phys. Rev. C* **103**, 034908 (2021).
35. Abdallah, M. S. et al. Disappearance of partonic collectivity in $\sqrt{s_{\rm NN}} = 3$ GeV Au+Au collisions at RHIC. *Phys. Lett. B* **827**, 137003 (2022).
36. Abbott, B. P., Abbott, R., Abbott, T. D. & Abraham, S. et al. GW190425: observation of a compact binary coalescence with total mass ~3.4$M_\odot$. *Astrophys. J. Lett.* **892**, L3 (2020).
37. Fonseca, E. et al. Refined mass and geometric measurements of the high-mass PSR J0740+6620. *Astrophys. J. Lett.* **915**, L12 (2021).
38. Cromartie, H. T. et al. Relativistic Shapiro delay measurements of an extremely massive millisecond pulsar. *Nat. Astron.* **4**, 72–76 (2020).
39. Tsang, C. Y., Tsang, M. B., Danielewicz, P., Lynch, W. G. & Fattoyev, F. J. Impact of the neutron-star deformability on equation of state parameters. *Phys. Rev. C* **102**, 045808 (2020).
40. Tolman, R. C. Static solutions of Einstein's field equations for spheres of fluid. *Phys. Rev.* **55**, 364–373 (1939).
41. Oppenheimer, J. R. & Volkoff, G. M. On massive neutron cores. *Phys. Rev.* **55**, 374–381 (1939).
42. Baym, G., Pethick, C. & Sutherland, P. The ground state of matter at high densities: equation of state and stellar models. *Astrophys. J.* **170**, 299 (1971).
43. Huth, S. et al. Constraining neutron-star matter with microscopic and macroscopic collisions. *Nature* **606**, 276–280 (2022).
44. Lattimer, J. M., Pethick, C. J., Prakash, M. & Haensel, P. Direct Urca process in neutron stars. *Phys. Rev. Lett.* **66**, 2701–2704 (1991).
45. Page, D., Lattimer, J. M., Prakash, M. & Steiner, A. W. Minimal cooling of neutron stars: a new paradigm. *Astrophys. J. Suppl. Ser.* **155**, 623 (2004).
46. Brown, E. F. et al. Rapid neutrino cooling in the neutron star MXB 1659-29. *Phys. Rev. Lett.* **120**, 182701 (2018).
47. Shternin, P. S., Yakovlev, D. G., Heinke, C. O., Ho, W. C. G. & Patnaude, D. J. Cooling neutron star in the Cassiopeia A supernova remnant: evidence for superfluidity in the core. *Mon. Not. R. Astron. Soc.* **412**, L108–L112 (2011).
48. Capano, C. D. et al. Stringent constraints on neutron-star radii from multimessenger observations and nuclear theory. *Nat. Astron.* **4**, 625 (2020).
49. Ghosh, S., Chatterjee, D. & Schaffner-Bielich, J. Imposing multi-physics constraints at different densities on the neutron star equation of state. *Eur. Phys. J. A* **58**, 37 (2022).
50. Drischler, C., Furnstahl, R. J., Melendez, J. A. & Phillips, D. R. How well do we know the neutron-matter equation of state at the densities inside neutron stars? A Bayesian approach with correlated uncertainties. *Phys. Rev. Lett.* **125**, 202702 (2020).
51. Drischler, C., Melendez, J. A., Furnstahl, R. J. & Phillips, D. R. Quantifying uncertainties and correlations in the nuclear-matter equation of state. *Phys. Rev. C* **102**, 054315 (2020).
52. Sorensen, A. et al. Dense nuclear matter equation of state from heavy-ion collisions. Prog. Part. Nucl. Phys. https://doi.org/10.1016/j.ppnp.2023.104080 (2022).
53. Li, B.-A., Chen, L.-W. & Ko, C. M. Recent progress and new challenges in isospin physics with heavy-ion reactions. *Phys. Rep.* **464**, 113–281 (2008).
54. Margueron, J., Hoffmann Casali, R. & Gulminelli, F. Equation of state for dense nucleonic matter from metamodeling. I. Foundational aspects. *Phys. Rev. C* **97**, 025805 (2018).
55. Dutra, M. et al. Relativistic mean-field hadronic models under nuclear matter constraints. *Phys. Rev. C* **90**, 055203 (2014).
56. Adamczewski-Musch, J. et al. Proton, deuteron and triton flow measurements in Au+Au collisions at $\sqrt{s_{\rm NN}} = 2.4$ GeV. *Eur. Phys. J. A* **59**, 80 (2023).
57. Pinkenburg, C. et al. Elliptic flow: transition from out-of-plane to in-plane emission in Au+Au collisions. *Phys. Rev. Lett.* **83**, 1295–1298 (1999).
58. Liu, H. et al. Sideward flow in Au+Au collisions between 2*A* and 8*A* GeV. *Phys. Rev. Lett.* **84**, 5488–5492 (2000).

59. Oliinychenko, D., Sorensen, A., Koch, V. & McLerran, L. Sensitivity of Au+Au collisions to the symmetric nuclear matter equation of state at 2–5 nuclear saturation densities. *Phys. Rev. C* **108**, 034908 (2023).
60. Bayes, T. & Price, R. An essay towards solving a problem in the doctrine of chance. By the late Rev. Mr. Bayes, communicated by Mr. Price, in a letter to John Canton, A. M. F. R. S. *Philos. Trans. R. Soc. Lond.* **53**, 370–418 (1763).

Acknowledgements

We would like to acknowledge many stimulating discussions with the participants at the workshops sponsored by the Institute of Nuclear Theory in 2021 and 2022 and with members of the Transport Model Evaluation Project. We are grateful to C. Drischler for providing the χEFT calculations shown in our figures. This work is supported in part by the National Science Foundation (Grant No. PHY-2209145 to R.K., W.G.L., C.Y.T. and M.B.T.) and the US Department of Energy, Office of Science, Office of Nuclear Physics (Grant No. DE-FG02-87ER40365 to C.J.H.). The Facility for Radioactive Ion Beams (FRIB), funded by the US Department of Energy, is committed to fostering a safe, diverse, equitable and inclusive work and research environment in which respect and personal integrity are valued. We adhere to the FRIB research code of conduct in accordance with the highest scientific, professional and ethical standards, as detailed in https://frib.msu.edu/users/pac/conduct.html. In an ideal world, it should not be necessary to identify the authors by gender or from under-represented group. Until the ideal world is reached, we acknowledge that our references and citations most likely under-represent contributions from women and minorities. We further acknowledge that Michigan State University occupies the ancestral, traditional and contemporary lands of the Anishinaabeg and the Three Fires Confederacy of the Ojibwe, Odawa and Potawatomi peoples. In particular, the university resides on land ceded in the 1819 Treaty of Saginaw.

Author contributions

C.Y.T. and M.B.T. first conceived the project. C.Y.T. wrote the software for the Bayesian analysis. C.Y.T., M.B.T. and W.G.L. collected and evaluated all the constraints used in the analysis. R.K. researched, reviewed and validated the final set of constraints adopted in Table 1. R.K. also wrote some of the software codes used to analyse the Bayesian results and generated all the figures with data. C.J.H. contributed to the impact of the Urca cooling section. All authors contributed to the writing, editing and revising of the manuscript. The ordering of the authors reflects the length of time the authors have joined the project.

Competing interests

The authors declare no competing interests.

Additional information

Supplementary information The online version contains supplementary material available at https://doi.org/10.1038/s41550-023-02161-z.

Correspondence and requests for materials should be addressed to ManYee Betty Tsang.

Peer review information *Nature Astronomy* thanks the anonymous reviewers for their contribution to the peer review of this work.